Finite-temperature properties of the antiferroelectric perovskite PbZrO₃ from a deep-learning interatomic potential

Huazhang Zhang [1,2,*], Hao-Cheng Thong [1,3] Louis Bastogne [1], Churen Gui [1,4] Xu He [1], and Philippe Ghosez [1,†]

[1]*Theoretical Materials Physics, Q-MAT, University of Liège, B-4000 Sart-Tilman, Belgium*
[2]*Department of Physics, School of Science, Wuhan University of Technology, Wuhan 430070, People's Republic of China*
[3]*State Key Laboratory of New Ceramics and Fine Processing, School of Materials Science and Engineering,*
Tsinghua University, Beijing 100084, People's Republic of China
[4]*Key Laboratory of Quantum Materials and Devices of Ministry of Education, School of Physics,*
Southeast University, Nanjing 211189, People's Republic of China

The prototypical antiferroelectric perovskite PbZrO₃ (PZO) has garnered considerable attention in recent years due to its significance in technological applications and fundamental research. Many unresolved issues in PZO are associated with large length- and time-scales, as well as finite temperatures, presenting significant challenges for first-principles density functional theory studies. Here, we introduce a deep-learnining interatomic potential of PZO, enabling investigation of finite-temperature properties through large-scale atomistic simulations. Trained using an elaborately designed dataset, the model successfully reproduces a large number of phases, in particular, the recently discovered 80-atom antiferroelectric *Pnam* phase and ferrielectric *Ima*2 phase, providing precise predictions for their structural and dynamical properties. Using this model, we investigated phase transitions of multiple phases, including *Pbam*/*Pnam*, *Ima*2, and *R*3*c*, which show high similarity to the experimental observation. Our simulation results also highlight the crucial role of free energy in determining the low-temperature phase of PZO, reconciling the apparent contradiction: *Pbam* is the most commonly observed phase in experiments, while theoretical calculations predict other phases exhibiting even lower energy. Furthermore, in the temperature range where the *Pbam* phase is thermodynamically stable, typical double polarization hysteresis loops for antiferroelectrics were obtained, along with a detailed elucidation of the structural evolution during the electric-field induced transitions between the nonpolar *Pbam* and polar *R*3*c* phases.

I. INTRODUCTION

Antiferroelectric (AFE) materials refer to a class of crystals that typically possesses local antiparallel dipoles, which forms a macroscopic nonpolar state, but can be turned into a polar state under the application of an electric field [1,2]. The electric-field induced nonpolar to polar switching gives rise to the peculiar double polarization-versus-electric field (*P-E*) hysteresis loop, which provides antiferroelectrics a series of functional properties that are highly appealing for applications [3–7]. Lead zirconate (PbZrO₃, PZO) was historically the first discovered antiferroelectric material, right after the concept proposed by Kittel in the early 1950s [8–10]. PZO has received considerable attention since then, primarily driven by the strong demand of applications, including energy storage, electromechanical actuation, electrocaloric effects, thermal switching, etc. [11–18].

However, many fundamental properties of PZO have remained not fully understood, particularly those related to large length- and time-scales and finite temperatures, e.g., the true ground state and the temperature-dependent phase diagram.

According to the experimental observations, the ground state of PZO was found to be a 40-atom antiferroelectric *Pbam* phase [*Pbam*-AFE40, Fig. 1(a)] [19], with a transition to the high-temperature cubic phase occurring at $T_\mathrm{C} \approx 505\,\mathrm{K}$ [9]. Some studies have also suggested a controversial intermediate phase within a narrow temperature range around T_C [20–25]. Recently, the traditional viewpoint regarding the *Pbam* ground state of PZO has even been challenged by theoretical discoveries of a ferrielectric *Ima*2 phase [*Ima*2-FiE, Fig. 1(b)] [26], and an 80-atom antiferroelectric *Pnam* phase [*Pnam*-AFE80, Fig. 1(c)] [27], which were found to exhibit lower energies than that of the *Pbam* phase. The physical properties of these newly predicted phases and their stability against temperature are yet to be clarified. While recent experimental observations have revealed the existence of *Ima*2-like structures locally in PZO [28,29], and the regions of which could be further coarsened under compressive strains [30], the possibility of the existence of the *Ima*2-FiE phase at a macroscopic scale remains unclear. This raises a specific question: how to reconcile the apparent contradiction between these two aspects, where theoretical predictions suggest a lower energy for *Ima*2-FiE, but experimental observations more commonly identify *Pbam*-AFE40 as the low-temperature structure of PZO?

Another aspect yet to be fully understood in PZO concerns its electric-field induced nonpolar-polar transitions, which

---

*Contact author: hzhang@uliege.be
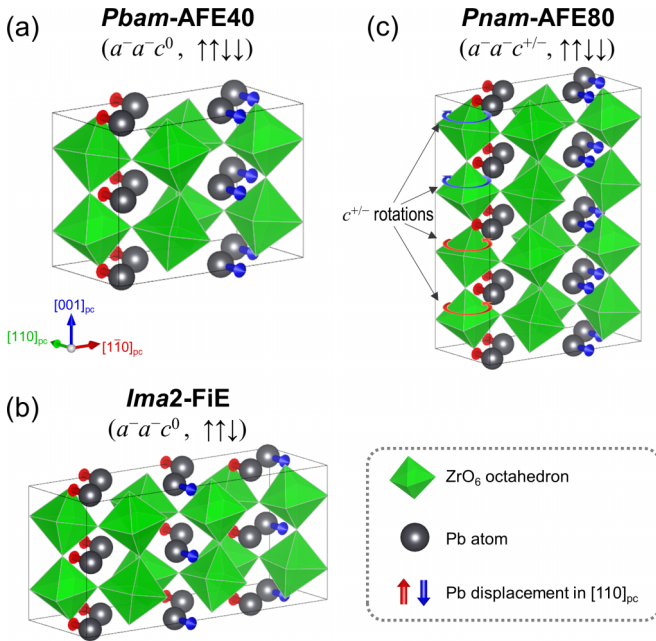†Contact author: philippe.ghosez@uliege.be

FIG. 1. Schematic views of the structures of (a) *Pbam*-AFE40, (b) *Ima*2-FiE, and (c) *Pnam*-AFE80 phases of PZO. The *Pbam*-AFE40 phase is featured by an octahedra rotation pattern $a^-a^-c^0$ and a fourfold periodic Pb displacement pattern "↑↑↓↓" in the pseudocubic [110] direction. The *Ima*2-FiE phase has a octahedra rotation pattern $a^-a^-c^0$ similar to that of the *Pbam*-AFE40 phase, but with a different threefold periodic Pb displacement pattern "↑↑↓" in the pseudocubic [110] direction. In the *Pnam*-AFE80 phase, the Pb displacement pattern is similar to that of the *Pbam*-AFE40 phase, but there are additional octahedra rotations around the c axis (pseudocubic [001]), alternating between in-phase and antiphase rotations, i.e., two layers of clockwise rotations followed by two layers of anticlockwise rotations, and so on. We refer to this alternating in-phase and antiphase c-rotation pattern as "$c^{+/-}$".

constitute the conceptual foundation for PZO being AFE and enable most of the functionalities of PZO-based materials. From theoretical calculation, polar $R3c$ and *Ima*2-FiE are found to be energetically very close to the nonpolar antiferroelectric *Pbam*-AFE40 phase (with energy differences around 1 meV/f.u. [26,31,32]), and thus become possible polar phases induced by electric field. Experimentally, however, a nonpolar to polar phase transition in PZO bulk samples (crystal or ceramic) is hardly reported since the electric field required is usually higher than the breakdown field [9,33]. Thus, most experimental studies on the electric-field induced phase transitions were conducted on PZO films [34–36] or PZO-based solid solutions [37–43]. However, the influences from strains, surfaces and foreign elements in films and solid solutions are usually significant and cannot be ignored. Given the fundamental importance of nonpolar-polar transitions in pure PZO and the experimental challenges with bulk materials, it is necessary and potentially feasible to study the electric-field induced transitions employing reliable theoretical methods. The outcomes would also be beneficial to the understanding and optimization of the performance of PZO-based materials and facilitate their applications.

The aforementioned issues in PZO could be resolved through theoretical investigations relying on a large configuration system, and its dynamical response to the external fields such as temperature and electric field. Although first-principles density function theory (DFT) calculation has been a successful atomistic simulation method for investigating PZO, it is computationally expensive for such dynamical simulation, especially for a system with more than hundreds of atoms. Molecular dynamics (MD) or Monte Carlo simulations using first-principles-based effective interatomic potentials have become an appealing solution, i.e., following the so-called "second-principles" approach [44]. Relevant efforts include the development of effective Hamiltonian and shell models for PZO [45–48]. However, the investigation of a system like PZO with a complex energy surface remains challenging, resulting poor prediction of certain crucial structures.

In recent years, machine learning methods have been introduced for constructing interatomic potentials, offering new solutions for highly accurate large-scale simulations that consider all atomistic degrees of freedom [49,50]. Particularly, the deep potential for molecular dynamics (DeePMD) has attracted significant attention [51]. Thanks to the development of the open-source DeePMD-kit software, this method is gaining increasing popularity in studies across a wide variety of systems, including water, metals, oxides, organic molecules, etc. [52–55]. For ferroelectric compounds, the deep potential approach has been successfully applied to $SrTiO_3$ [56], $KNbO_3$ [57], $PbTiO_3$ [58], $Pb(Zr, Ti)O_3$ [59], HfO_2 [60], $PbTe$ [61], In_2Se_3 [62], bilayered BN [63], etc. Recently, a modular development scheme for deep potential in complex solid solutions was proposed [64], and a universal model for perovskite oxides involving 14 metal elements was presented [65]. Regarding the antiferroelectric PZO, despite its highly complex potential energy surface, given the success of previous applications, employing the deep potential method appears very promising for developing a highly accurate interatomic potential.

In this work, we developed a deep-learning interatomic potential of PZO for finite-temperature simulation. The model, which is trained with an elaborately designed training set, can accurately reproduce numerous phases in PZO and provide precise predictions on their properties. Notably, the model successfully captures the recently discovered *Pnam*-AFE80 and *Ima*2-FiE phases. The model is thoroughly validated and utilized for investigating the finite-temperature properties through molecular dynamic simulations. The simulations successfully reproduce the temperature-dependent phase transitions and double *P-E* loops, showing good agreement with experiments. Additionally, the simulations also provide insights into why PZO tends to adopt the *Pbam*-AFE40 as its room-temperature phase, rather than other low energy phases like *Ima*2-FiE. We prospect that this model will serve as a useful tool for studying PZO, offering opportunities for new insights into this fascinating material.

II. METHODOLOGY

A. First-principles calculations

The first-principles DFT calculations were performed using the ABINIT software [66–69], employing the GGA-PBEsol

functional [70] and a planewave-pseudopotential approach with optimized norm-conserving pseudopotentials from the PseudoDojo server [71,72]. The energy cutoff for the plane-wave expansion was 60 Ha, and the Brillouin zone sampling was equivalent or denser to a $6\times6\times6$ k-point grid for the five-atom perovskite unit cell. The electronic self-consistent cycles were converged until the potential residual is smaller than 10^{-18} Ha. Structural relaxations were performed based on the Broyden-Fletcher-Goldfarb-Shanno minimization algorithm until the forces are less than 10^{-6} Ha/Bohr and the stresses are less than 10^{-8} Ha/Bohr^3. The Born effective charges, phonon dispersions, and elastic and piezoelectric tensors were calculated according to the density functional perturbation theory (DFPT) as implemented in ABINIT and analyzed using the ANADDB tool [73].

For building the training set, we used a less stringent convergence criterion for the electronic self-consistent cycles of 10^{-10} Ha on the potential residual to facilitate the acquisition of the data. We also developed a plugin for the dpdata package to convert the data format [74], so that the DeePMD-kit can make use of the ABINIT results to train models.

B. Second-principles calculations

1. Model training

The deep-learning interatomic potential model for PZO was trained using the open-source package DeePMD-kit [75,76]. The deep potential method assumes that the total energy of a system is the summation of the energy contributions from each of the atoms, whereas the energy contribution from each atom is determined by its local environment within a cutoff radius and can be parameterized with neural networks. To build the PZO model, the cutoff radius was set to be 9.0 Å, smoothing from 1.5 Å. The embedding and fitting networks both have three layers, with the size of (25, 50, 100) and (240, 240, 240), respectively. The loss function is defined by

$$L = p_e (\Delta e)^2 + p_f \frac{\sum_i |\Delta f_i|^2}{3N} + p_\xi \frac{\|\Delta \xi\|^2}{9}, \qquad (1)$$

where Δ denotes the difference between the model predictions and the training data, e is the energy per atom, f_i is the force vector on the atom i, and N is the number of atoms, ξ is the virial. The p_e, p_f, and p_ξ are the prefactors which balance the losses in energy, forces and virials, respectively. The p_e and p_ξ increase from 0.02 to 1, and p_f decreases from 1000 to 1 during the training procedure.

2. Model-based calculations

The model-based calculations were carried out using LAMMPS [77,78] with periodic boundary conditions. Structural relaxations were performed based on the conjugate gradient algorithm, with the convergence criterion on forces of 5×10^{-3} eV/Å. Phonon dispersion curves were calculated based on the finite difference method, using Phonopy [79] to analyze the force set produced by the model and extracted by LAMMPS. The nonanalytical corrections for the phonon dispersions were conducted using the Born effective charges of the corresponding phases from DFPT calculations. The elastic and piezoelectric tensors were calculated by analyzing the stress and polarization changes to strain

perturbations, respectively, with the atomic positions fully relaxed. The finite-temperature MD simulations were performed using NPT ensemble, with the temperature and pressure controlled by a Nose-Hoover thermostat and barostat. The electric field was applied by adding on each of the atoms extra forces according to $f_{i,\alpha} = \sum_\beta Z^*_{i,\alpha,\beta} E_\beta$, where Z^* is the Born effective charges in the cubic reference phase, E is the applied electric field, the subscript i is the index of atoms, and α, β denote the Cartesian directions x, y, and z. The time step for the MD simulations is 1 fs. At each temperature, the system was first equilibrated for 50 ps, then the simulation continued for another 50 ps for property analysis. The MD trajectories were analyzed with Agate [80]. In particular, the polarization was calculated based on the Born effective charge of the cubic phase using the algorithm implemented in Agate.

III. SECOND-PRINCIPLES MODEL

A. Training set design

PZO probably has one of the most complex potential energy surfaces of all perovskite oxides. As can be seen from the phonon dispersion curves of its cubic parent phase [Fig. 2(a)], lattice instabilities are present throughout the whole Brillouin zone. The strongest instabilities include the polar modes at Γ, and the in-phase and antiphase oxygen octahedra rotations at M and R. Additionally, there are also unstable modes at X, M, and R points, which are featured by the antipolar motions of cations. By successively condensing unstable modes in the cubic parent phase, PZO can reach various stationary phases. Figure 2(b) and Table I provide a series of stationary phases of PZO, where the cubic parent phase is taken as the energy reference. It is worth noticing that not only the number of different phases in PZO is considerably large, but also many of them are very close in energy. So, it seems quite challenging to capture such a large number of competing phases within a single interatomic effective potential model.

Thanks to the powerful descriptive capability of neural networks, it is possible to overcome this challenge by constructing a comprehensive training set covering as many phases as possible. Then, to prevent over-inflating the training set, an efficient strategy for sampling the potential energy surface is also essential. Therefore, in contrast to the commonly used methods of concurrently and automatically sampling the potential energy surface from molecular dynamics [81], we construct our training set for PZO through smart design. We herein briefly illustrate our strategy for the training set design in Figs. 3(a) and 3(b), and more general considerations are presented elsewhere [82]. To build the training set, we first condense different unstable lattice modes in the cubic reference structure either individually or jointly, and obtain a series of stationary phases, which are corresponding to the local minima or saddle points on the potential energy surface. Then, we make linear interpolations and extrapolations between different phases (including the cubic reference phase and the explored distorted phases), and put the interpolating and extrapolating paths into the training set. Finally, we also include in the training set noisy configurations, which were obtained by populating phonon modes at various temperatures
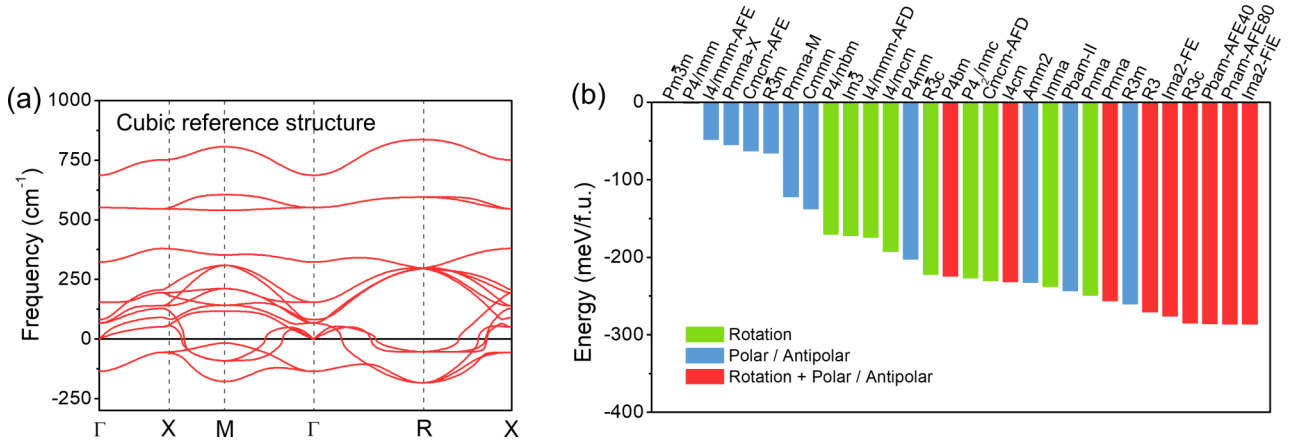
FIG. 2. Exploration of potential energy surface of PZO by first-principles calculations. (a) Phonon dispersions of PZO in the cubic reference structure. (b) Energies of various stationary phases of PZO, where the cubic phase is taken as the energy reference.

and imposing random strains around each of those phases (the algorithm is implemented in Agate). The final training set used for training the PZO model contains 12 812 configurations in total. The energy distribution of the configurations is presented in Fig. 3(c).

B. Model validations

1. Training set and test set

We first validate the model by examining its reproducibility on both the training set and a test set. As shown in

TABLE I. Space group, lattice distortions and calculated energies of various phases of PZO. For the lattice distortions, only the dominant antiferrodistortive (AFD) rotations and polar/antipolar cation motions are presented. The DFT and model energies are reported in relative values with respect to the cubic reference structure.

|	Phase	Space group (No.)	AFD rotation	Polar/antipolar	DFT energy (meV/f.u.)	Model energy (meV/f.u.)
1	$Pm\bar{3}m$	$Pm\bar{3}m$ (221)			0.0	0.0
2	$P4mm$	$P4mm$ (99)		FE[1 0 0]	−202.9	−208.7
3	$Amm2$	$Amm2$ (38)		FE[1 1 0]	−232.8	−235.9
4	$R3m$	$R3m$ (160)		FE[1 1 1]	−260.7	−263.9
5	$Pmma$-X	$Pmma$ (51)		AFE[1 0 0] ($q = [0, 0, 1/2]$)	−55.1	−56.2
6	$Cmcm$-AFE	$Cmcm$ (63)		AFE[1 1 0] ($q = [0, 0, 1/2]$)	−63.4	−64.0
7	$Cmmm$	$Cmmm$ (65)		AFE[1 0 0] ($q = [1/2, 1/2, 0]$)	−138.0	−141.5
8	$Pmma$-M	$Pmma$ (51)		AFE[1 1 0] ($q = [1/2, 1/2, 0]$)	−122.6	−129.4
9	$P4/nmm$	$P4/nmm$ (129)		AFE[0 0 1] ($q = [1/2, 1/2, 0]$)	−2.0	−3.3
10	$I4/mmm$-AFE	$I4/mmm$ (139)		AFE[1 0 0] ($q = [1/2, 1/2, 1/2]$)	−48.5	−50.1
11	$R\bar{3}m$	$R\bar{3}m$ (166)		AFE[1 1 1] ($q = [1/2, 1/2, 1/2]$)	−66.1	−68.6
12	$P4/mbm$	$P4/mbm$ (127)	$a^0a^0c^+$		−170.8	−179.2
13	$I4/mcm$	$I4/mcm$ (140)	$a^0a^0c^-$		−192.9	−192.1
14	$I4/mmm$-AFD	$I4/mmm$ (139)	$a^+a^+c^0$		−174.6	−186.4
15	$Cmcm$-AFD	$Cmcm$ (63)	$a^+b^-c^0$		−230.5	−229.3
16	$Imma$	$Imma$ (74)	$a^-a^-c^0$		−238.1	−239.8
17	$Im\bar{3}$	$Im\bar{3}$ (204)	$a^+a^+a^+$		−172.4	−181.7
18	$P4_2/nmc$	$P4_2/nmc$ (137)	$a^+a^+c^-$		−227.1	−226.9
19	$Pnma$	$Pnma$ (62)	$a^-a^-c^+$		−249.4	−249.4
20	$R\bar{3}c$	$R\bar{3}c$ (167)	$a^-a^-a^-$		−222.5	−227.2
21	$P4bm$	$P4bm$ (100)	$a^0a^0c^+$	FE[0 0 1]	−224.9	−221.6
22	$I4cm$	$I4cm$ (108)	$a^0a^0c^-$	FE[0 0 1]	−231.8	−225.8
23	$R3$	$R3$ (146)	$a^+a^+a^+$	FE[1 1 1]	−271.1	−272.2
24	$R3c$	$R3c$ (161)	$a^-a^-a^-$	FE[1 1 1]	−285.3	−290.3
25	$Ima2$-FE	$Ima2$ (46)	$a^-a^-c^0$	FE[1 1 0]	−276.5	−277.0
26	$Pmna$	$Pmna$ (53)	$a^-a^-c^0$	AFE[1 1 0] ($q = [1/2, −1/2, 0]$)	−256.6	−256.2
27	$Pbam$-II	$Pbam$ (55)		AFE[1 1 0] ($q = [1/4, −1/4, 0]$)	−243.6	−247.7
28	$Pbam$-AFE40	$Pbam$ (55)	$a^-a^-c^0$	AFE[1 1 0] ($q = [1/4, −1/4, 0]$)	−285.9	−286.3
29	$Pnam$-AFE80	$Pnam$ (62)	$a^-a^-c^{+/-}$	AFE[1 1 0] ($q = [1/4, −1/4, 0]$)	−286.4	−286.8
30	$Ima2$-FiE	$Ima2$ (46)	$a^-a^-c^0$	AFE[1 1 0] ($q = [1/3, −1/3, 0]$)	−286.7	−286.3
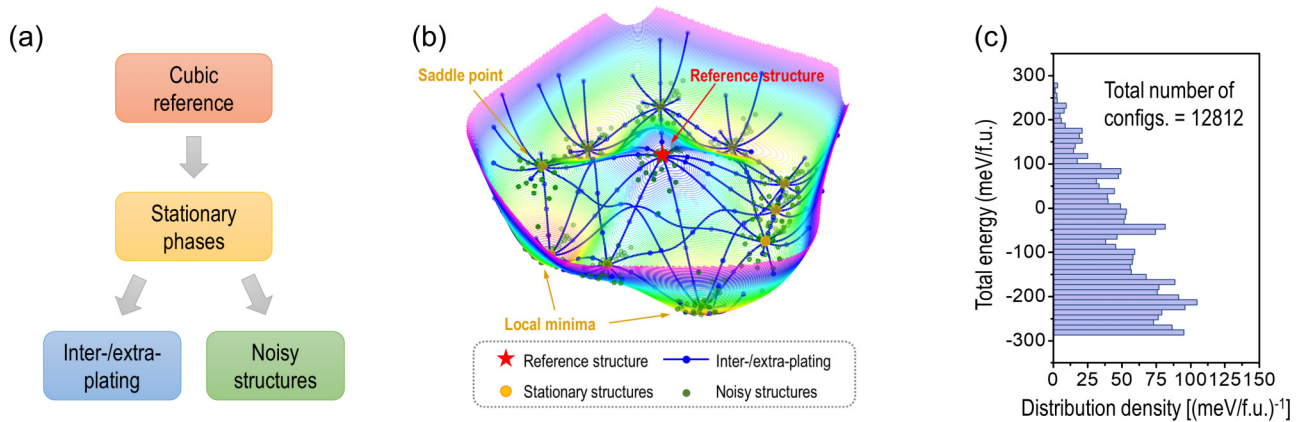
FIG. 3. Training set design. (a) Procedures of sampling the potential energy surface and constructing the training set. (b) Schematic plot of sampling the potential energy surface. (c) Energy distribution of the configurations in the training set.

Figs. 4(a)–4(c), our model achieves high-quality fittings on the energy, forces and virials ($R^2 > 0.997$) for the configurations in the training set. This can be attributed to the powerful descriptive capability of the neural networks. To ensure that the model does not demonstrate significant overfitting, we construct a test set by randomly selecting 255 configurations from MD trajectories at various temperatures (100, 200, 300, 500, and 800 K) and feed them back into DFT calculations. Figures 4(d)–4(f) provide comparisons of the energy, forces and virials for the configurations in the test set. The model also exhibits a high level of reproducibility for the data not in

the training set ($R^2 > 0.993$), indicating a satisfactory generalization ability of the model.

2. Stationary phases

We subsequently validate the model by performing structural relaxations of various stationary phases, to ensure that the corresponding stationary points on the potential energy surface are accurately described. Due to the generality of our training set, the trained model effectively captures no less than 30 different phases. Not only the energy [Fig. 5(a)
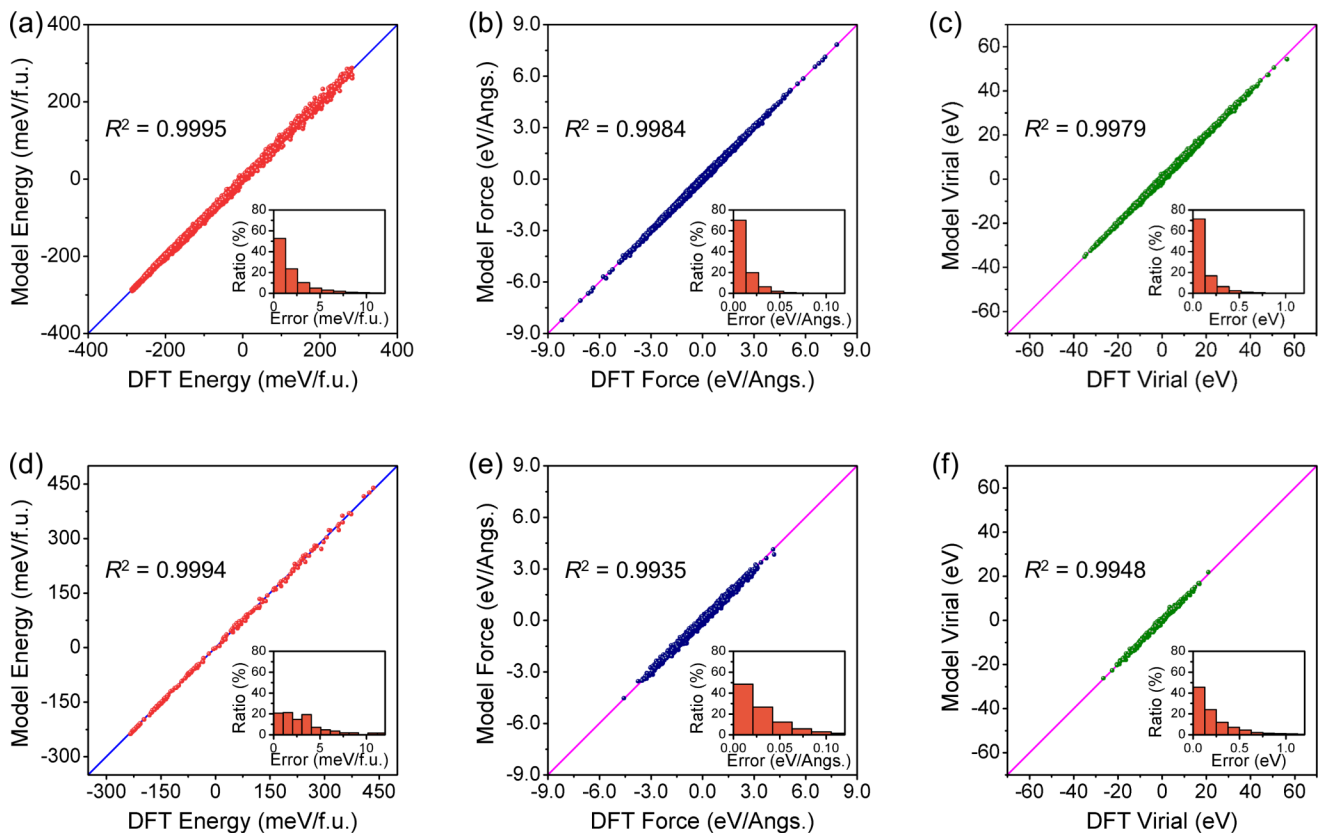

FIG. 4. Model validations on (a)–(c) training set and (d)–(f) test set. Comparisons of (a) and (d) energy, (b) and (e) forces, and (c) and (f) virials between DFT calculations and model predictions. The insets show the distributions of absolute errors.
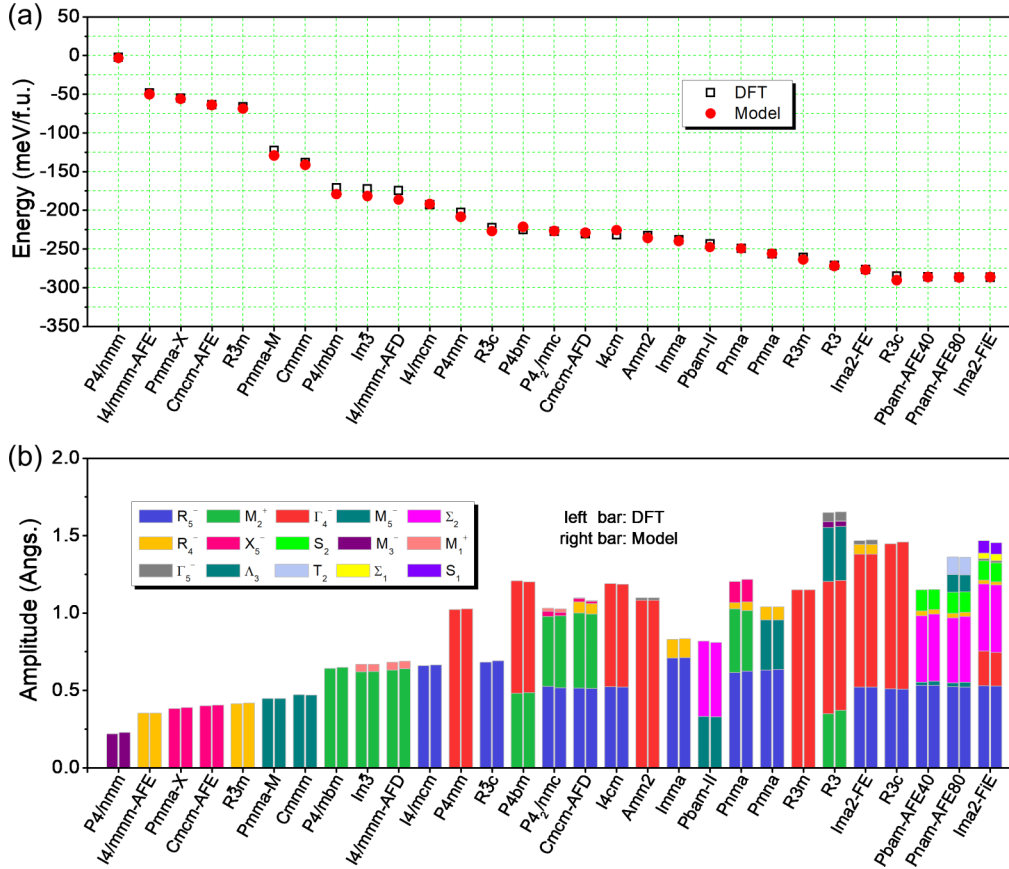
FIG. 5. Model validations by structural relaxations of different phases, which are corresponding to the stationary points on the potential energy surface. Comparisons of (a) energy and (b) lattice distortions between DFT calculations and model predictions. The cubic phase is taken as the energy reference.

and Table I], but also the lattice parameters (Table II in Appendix) and atomic distortions [Fig. 5(b)] obtained from the model-based structural relaxations are highly consistent with the results obtained from the first-principles relaxations. In particular, the recent reported *Pnam*-AFE80 and *Ima*2-FiE phases are successfully captured. This demonstrates that the model is quite efficient in describing the energy landscape.

Nevertheless, there are a few imperfections in the model, particularly the over stabilization of the *R*3*c* phase by about 5.0 meV/f.u., leading to a state that exhibits 3–4 meV/f.u. below the *Pbam*-AFE40, *Pnam*-AFE80, and *Ima*2-FiE phases, which should supposedly be above them. Although this changes the prediction of ground state at zero Kelvin, it does not significantly impact the simulation of the finite-temperature properties, as will be discussed later. In fact, the energies of these competing low-energy phases are too close to be distinguished within the accuracy of the model and should be considered as nearly degenerated. We notice that at the DFT level, the exact energy order of these phases already strongly depends on the employed exchange-correlation functional [26,32].

3. Second-order energy derivatives

We further validate the model by calculating the quantities of the second-order energy derivatives, i.e., the phonon frequencies, the elastic and piezoelectric tensors, which are corresponding to the curvatures of the potential energy surface around the stationary points. The calculations were performed on some important phases, including *Pm*$\bar{3}$*m* (parent cubic phase), *Pbam*-AFE40 (conventional antiferroelectric phase), *Pnam*-AFE80 (newly discovered antiferroelectric phase), *Ima*2-FiE (ferrielectric phase, the DFT ground state), *R*3*c* (electric-field induced ferroelectric phase), and *Imma* phase (the common parent phase of *Pbam*-AFE40, *Pnam*-AFE80, *Ima*2-FiE, and *R*3*c* phases). As illustrated in Fig. 6 and Tables III and IV, the model provides quite good agreements with the DFPT calculations on these second-order energy derivative quantities.

From Fig. 6, we see that the high-symmetry *Pm*$\bar{3}$*m* and *Imma* phases exhibit unstable phonon branches [Figs. 6(a) and 6(b)], highlighting that they are dynamically unstable at zero Kelvin, while the *R*3*c*, *Ima*2-FiE, and *Pnam*-AFE80 phases are free of lattice instability [Figs. 6(c), 6(e) and 6(f)]. For the *Pbam*-AFE40, one imaginary frequency at the *Z* point can still be observed from both DFPT and model-based calculations [Fig. 6(d)], which is in line with the recent discovery by Baker *et al.* [27]. By condensing this *Z*-point instability, the *Pbam*-AFE40 phase will change to the *Pnam*-AFE80 phase.

One potential concern with the model is the treatment of long-range dipole-dipole interactions. It is generally believed that the long-range dipole-dipole interactions are crucial for insulators, and ferroelectric-related phenomena are believed to arise from the delicate balance between long-range and
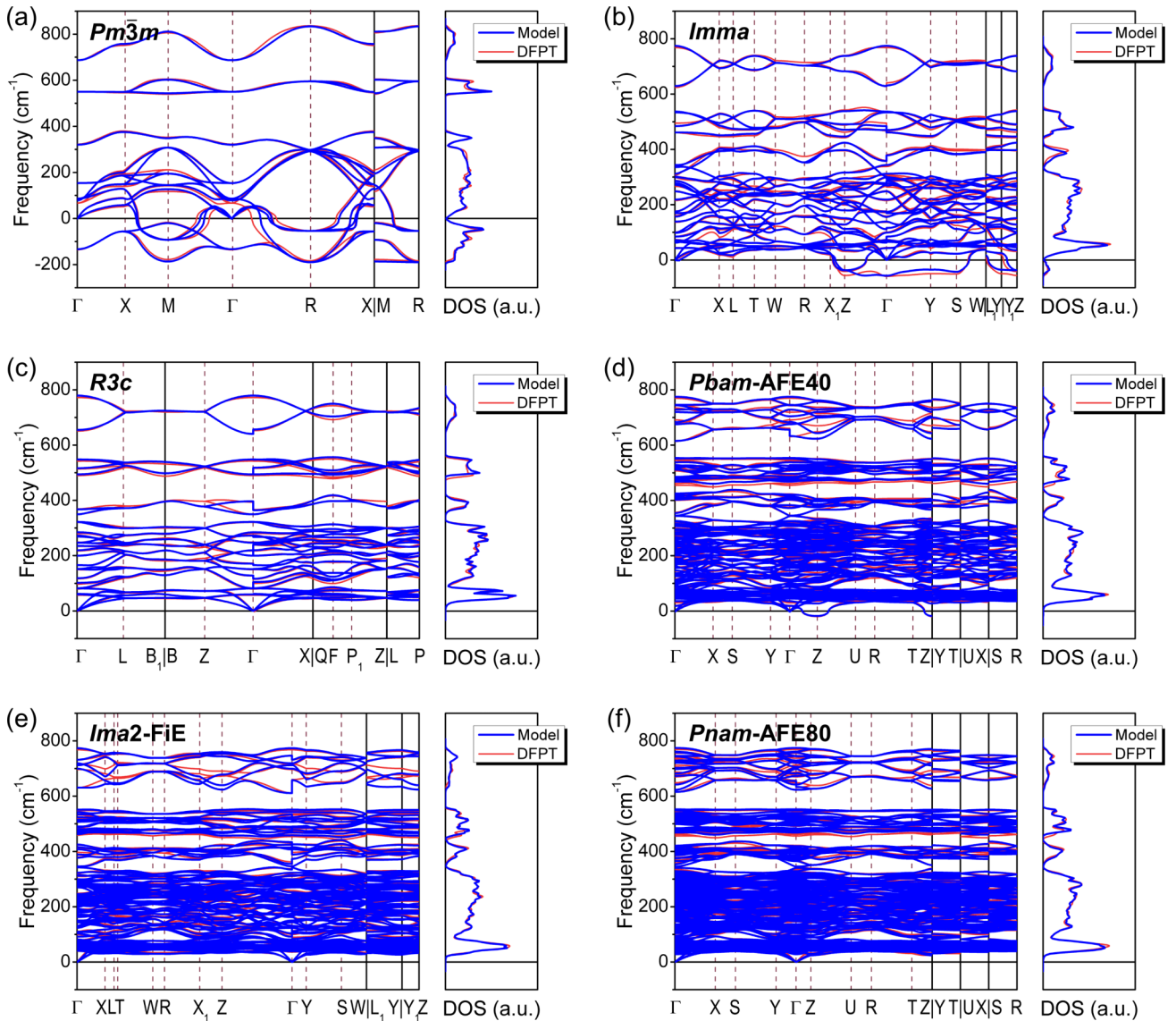
FIG. 6. Model validations by comparisons of phonon dispersions and phonon density of states calculated from DFPT and the model for different phases of PZO: (a) $Pm\bar{3}m$, (b) $Imma$, (c) $R3c$, (d) $Pbam$-AFE40, (e) $Ima2$-FiE, and (f) $Pnam$-AFE80.

short-range interactions [83]. However, for the model constructed in this work, there is no separation of the long-range and short-range interactions, but the total interactions were treated as a whole and truncated up to a cutoff radius (9 Å, roughly two times of the cubic cell parameter). This suggests that long-range effects might not be so important as initially thought, and some of them may have been effectively incorporated into the current description. It would be interesting to investigate how the treatment of long-range interactions from other approaches can affect the model [84].

IV. FINITE-TEMPERATURE PROPERTIES

A. Phase transitions

With the model thoroughly validated, it can be applied to investigate finite-temperature properties of PZO. Our initial objective is to simulate the temperature dependent phase transitions. Prior to presenting the results from our model, we will

briefly review the experimental facts and the outcomes from previous effective models on PZO.

Experimentally, PZO undergoes a phase transition from the low-temperature $Pbam$-AFE40 phase to the high-temperature cubic phase at $T_C \approx 505$ K [9]. In addition, within a narrow temperature region around T_C, some experimental studies have identified traces of a potential intermediate phase, while the exact nature of which is still under debate.

Theoretically, various effective models have been developed to simulate the finite-temperature behaviors of PZO. Gindele *et al.* [47] developed a shell model for the solid solution Pb(Zr, Ti)O$_3$, in which the antiferroelectric transition of pure PZO is successfully described. The model predicts the transition occurs around 420 K, slightly underestimated as compared to the experimental value. In a different approach, Mani *et al.* [45] developed an effective Hamiltonian model for PZO, which successfully describes the antiferroelectric phase transition as well as the behaviors under electric field and mechanical pressure. However, their model significantly
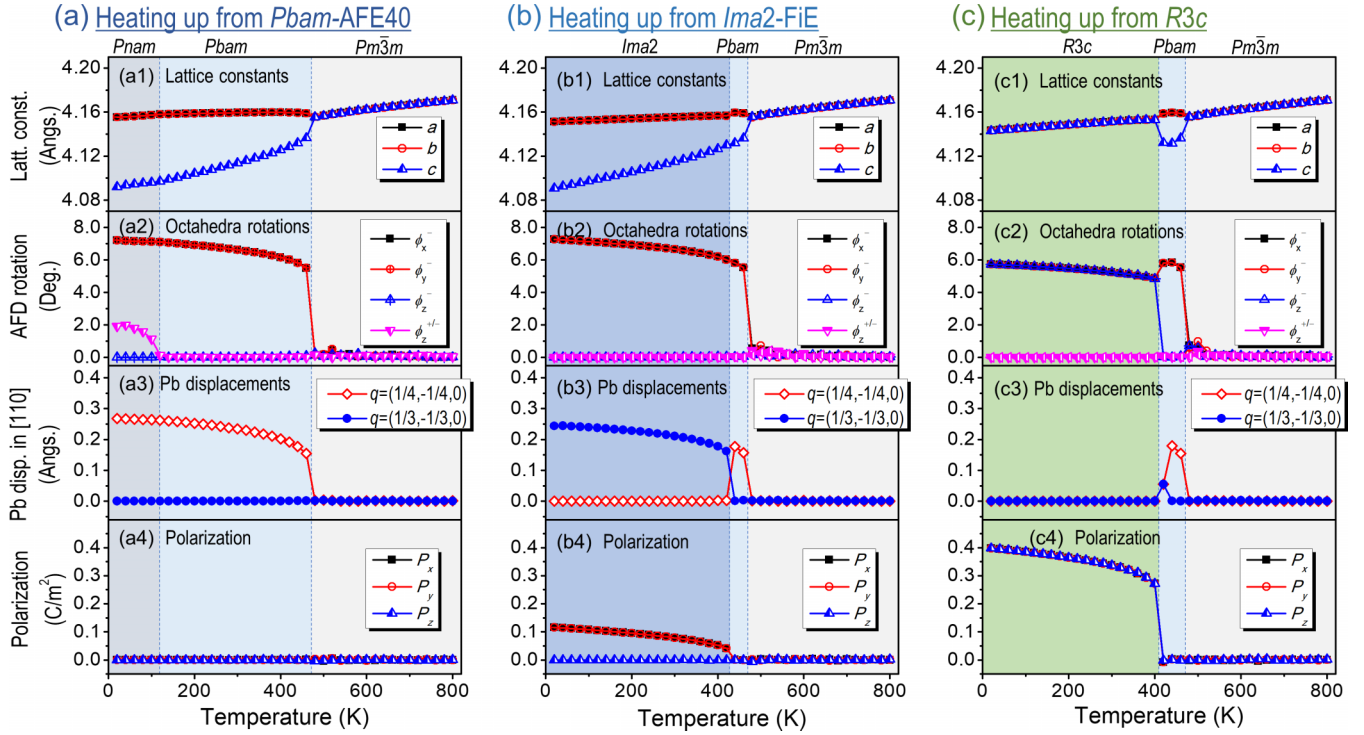
FIG. 7. Finite-temperature phase transitions during heating up from different homogeneous phases. The initial structures are in (a) *Pbam*-AFE40, (b) *Ima*2-FiE, and (c) *R*3*c*-FE phases. For each case, the four panels show the lattice constants, oxygen octahedra rotations, Pb displacements, and polarization as functions of temperature, respectively. The Pb displacements are first projected to pseudocubic [110] direction and then decomposed by different modulation wave vectors. The simulations were performed using $12 \times 12 \times 12$ supercells.

overestimates the transition temperature to 946 K. Independently, Patel *et al.* [46] reported another effective Hamiltonian model for PZO, in which a bilinear energetic coupling term between Pb motions and the oxygen octahedra rotations is introduced. This model well reproduces the low-temperature *Pbam*-AFE40 phase and the high-temperature cubic phase. Interestingly, between these two phases, the model predicts an intermediate phase, occurring within the temperature range from 650 to 1300 K. This intermediate phase is also in *Pbam* space group and characterized with similar "↑↑↓↓" Pb displacement pattern as in the low-temperature *Pbam*-AFE40 phase, but without the oxygen octahedra rotations (corresponding to the *Pbam*-II phase in Table I). In general, all these existing models mainly focus on the low-temperature *Pbam*-AFE40 phase and the antiferroelectric phase transition to the high-temperature cubic phase, with less consideration given to other potential metastable phases.

A prominent advantage of our model is the capability of describing a large number of metastable phases, and some of them exhibit similarly low energies and may potentially compete with each other. Our particular interest is to investigate how these competing low-energy phases behave at finite temperatures. Therefore, we performed MD simulations heating up from different homogeneous phases, i.e., *Pbam*-AFE40 (*Pnam*-AFE80), *Ima*2-FiE, and *R*3*c*, respectively, as well as cooling down from the high-temperature cubic phase. If not otherwise specified, our calculations employ $12 \times 12 \times 12$ repetitions of the five-atom perovskite unit cell as the simulating supercell, which is commensurate with *Pbam*-AFE40, *Pnam*-AFE80, *Ima*2-FiE, and *R*3*c*, so as

to avoid the bias arising from incompatibility in structural periodicity.

1. Heating

When the MD simulation starts heating from the *Pbam*-AFE40 phase, as shown in Fig. 7(a), the structure automatically goes to the *Pnam*-AFE80 phase at very low temperature (e.g., 20 K). This can be evidenced from the nonzero value of $\phi_z^{+/-}$ [Fig. 7(a2)]. Here, we use $\phi_z^{+/-}$ as an indicator to distinguish the *Pnam*-AFE80 and *Pbam*-AFE40 phases, which represents the octahedra rotations around the *z* axis with a complex pattern alternating between in-phase and antiphase rotations [Fig. 1(c)]. It is not surprising that when using *Pbam*-AFE40 as the initial configuration, it immediately transforms into *Pnam*-AFE80, due to condensation of the lattice instability at *Z* point. With increasing temperature upon 120 K, the *Pnam*-AFE80 transforms back to the *Pbam*-AFE40.

When heating up to 480 K, the system changes from the *Pbam*-AFE40 to cubic *Pm*$\bar{3}$*m* phase, along with the vanishing of the octahedra rotations ($a^- a^- c^0$, indicated by $\phi_x^- = \phi_y^- \neq 0$ and $\phi_z^- = 0$) and the antipolar Pb displacements [↑↑↓↓, indicated by $q = (1/4, -1/4, 0)$]. We do not observe any clear evidence for possible intermediate phase between *Pbam*-AFE40 and the cubic phase during the heating process. The *Pbam*-AFE40 to *Pm*$\bar{3}$*m* phase transition temperature observed at 480 K is quite close to the experimental transition temperature $T_C^{\text{exp.}} \approx 505$ K [9], showing a remarkable improvement on the estimation of the transition temperature compared to previous atomistic simulations [45–47].
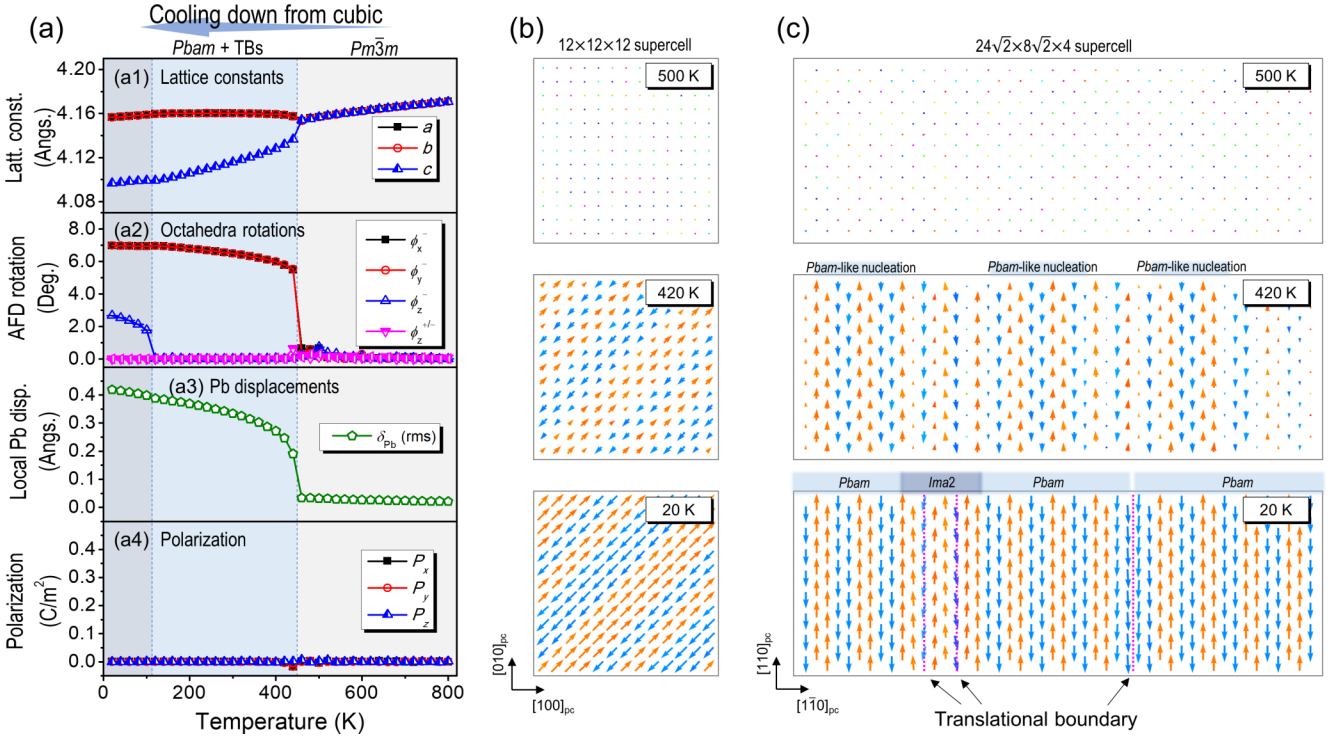
FIG. 8. Phase transitions and evolution of polarization patterns during cooling down from the cubic phase. (a) Changes of lattice constants, oxygen octahedra rotations, Pb displacements, and polarization with temperature. The Pb displacements were characterized by the root-mean-squared displacement with respect to the average position of the 12 surrounding oxygen atoms. (b) and (c) Local Pb displacement maps from the average structures at different temperatures during the cooling simulation. The arrows represent local Pb displacements with respect to the average position of the 12 surrounding oxygen atoms, with colors indicating directions. The simulations of (a) and (b) were performed using a $12 \times 12 \times 12$ supercells, and the simulations of (c) were performed using a $24\sqrt{2} \times 8\sqrt{2} \times 4$ supercell.

When the MD simulations start heating from the $Ima2$-FiE [Fig. 7(b)] or $R3c$ [Fig. 7(c)] phases, respectively, we found that these phases remain stable at low temperatures, in line with the fact that their phonon dispersions are free of structural instability. Furthermore, our simulations show that the thermal stability of the $Ima2$-FiE and $R3c$ phases is quite considerable, as they can be maintained to above room-temperature. This result also implies that there are considerable energy barriers between $Ima2$-FiE and $Pbam$-AFE40 and between $R3c$ and $Pbam$-AFE40. During heating, the $Ima2$-FiE and $R3c$ first transform into $Pbam$-AFE40 phase around 440 and 420 K [85], respectively, and then the $Pbam$-AFE40 changes to the cubic $Pm\bar{3}m$ phase around 480 K. It is very interesting to observe that the phase transition into $Pbam$-AFE40 always occurs in prior to the cubic phase. Unfortunately, there exists no experimental data for comparison with these simulation predictions so far, probably due to the difficulty of preparing PZO samples in pure $R3c$ or $Ima2$ phases.

2. Cooling

We also make use of the model to simulate phase transitions during cooling process. It seems that the simulation of cooling down from the cubic phase is more complicated compared to the simulations of heating up from homogeneous phases. The complexity arises due to the competition among the nearly degenerated low-energy phases, and the possible

emergence of domain walls or phase boundaries during the cooling process. Nevertheless, the cooling simulation hold the significance of helping to understand the formation of experimental room-temperature phase after high-temperature synthesis or thermal treatment. In PZO, the most commonly observed room-temperature phase is the $Pbam$-AFE40, but the DFT calculations predicts that some other phases like $Ima2$-FiE would exhibit lower energies. Why PZO prefers to select the $Pbam$-AFE40 as its room-temperature phase rather than other low-energy phases? This is a specific question that we want to address through the cooling simulations.

Considering the complexity and the inherent stochasticity of the cooling process, we repeated the cooling simulations from the 800 K (cubic phase) to 20 K for several times in supercells of different sizes. Figures 8(a) and 8(b) present the results from a $12 \times 12 \times 12$ supercell. The high-symmetry cubic structure go through phase transition below 460 K, along with the appearance of octahedra rotations $a^-a^-c^0$ ($\phi_x^- = \phi_y^- \neq 0$ and $\phi_z^- = 0$) and Pb off-centering displacements, while the system stays as nonpolar during the whole cooling process ($P_x = P_y = P_z = 0$). The transition temperature during cooling is slightly lower than that during heating, indicating the presence of thermal hysteresis, which in line with the fact that the antiferroelectric transition in PZO is of first order. After cooled down to low temperatures, the final Pb displacement pattern is "↑↑↑↑↓↓↑↑↓↓↓↓" [Fig. 8(b)], which is different from those in $Pbam$-AFE40 (↑↑↓↓), $Ima2$-FiE

($\uparrow\uparrow\downarrow$), or $R3c$ ($\uparrow\uparrow\uparrow\uparrow$), but can be viewed as *Pbam*-AFE40 with two translational boundaries (TBs) [28,86]. Besides, an increase in ϕ_z^- at the low-temperature end is also observed [Fig. 8(a2)]. Upon closer inspection of the low-temperature structure, we find that the nonzero ϕ_z^- appears locally in the regions exhibiting the "$\uparrow\uparrow\uparrow\uparrow$" and "$\downarrow\downarrow\downarrow\downarrow$," indicating a tendency toward $R3c$. Nevertheless, the emergence of ϕ_z^- depends specifically on the Pb displacement pattern and will disappear in simulations using a supercell of a different size.

We repeat the cooling simulation in a $24\sqrt{2}\times8\sqrt{2}\times4$ supercell, which allows for a better view of more columns of dipoles [Fig. 8(c)]. The changes in lattice parameters, octahedra rotations, and polarization are almost identical to those observed in the simulation using a $12\times12\times12$ supercell, except for the absence of an increase in ϕ_z^- at the low-temperature end. After cooling down to very low temperature, we find that the prevalence of the $\uparrow\uparrow\downarrow\downarrow$ fragments of Pb displacement pattern is quite noteworthy. This confirms that the final structure is indeed the *Pbam*-AFE40 phase with translational boundaries. In this view, the simulation results agree well with the experimental fact that the most commonly observed low-temperature phase of PZO is the *Pbam*-AFE40 phase.

A careful inspection of the evolution of local Pb displacements reveals the detailed process of evolution of the Pb displacement pattern during cooling. At the temperature just below T_C, *Pbam*-like "$\uparrow\uparrow\downarrow\downarrow$" domains first nucleate in different regions of PZO [Fig. 8(c), 420 K]. Subsequently, as the temperature decreases, *Pbam* domains gradually expand and eventually occupy almost the entire crystal. Finally, these *Pbam* domains with $\uparrow\uparrow\downarrow\downarrow$ polar patterns are frozen down to low temperatures [Fig. 8(c), 20 K], while the global transition to other patterns like *Ima*2-FiE ($\uparrow\uparrow\downarrow$), or $R3c$ ($\uparrow\uparrow\uparrow\uparrow$) is kinetically hindered due to the energy barriers between those phases. The key reason why PZO tends to be in *Pbam*-AFE40 phase at room-temperature is most likely due to the early appearance of *Pbam*-like structures just below T_C. Namely, at the temperature just below T_C, the *Pbam*-AFE40 holds the advantage in free-energy over other phases such as *Ima*2-FiE or $R3c$. Aramberri *et al.* [26] previously made a similar statement, where they estimated the phonon entropy and free-energy using harmonic approximation. It is encouraging that the statement can now be more directly demonstrated through atomistic simulations. Our results emphasize the significance of free-energy, rather than the internal energy at zero Kelvin, as a critical factor in determining the actual low-temperature phase in PZO.

In addition to the prevalent "$\uparrow\uparrow\downarrow\downarrow$" polar patterns, the "$\uparrow\uparrow\downarrow$" patterns can also be observed in the region of translational boundaries, which closely resembles the structure of the *Ima*2-FiE phase [Fig. 1(b)]. This result is aligned surprisingly well with the recent experimental microscopic observation by Liu *et al.* [28], who found that in PZO single crystal the *Ima*2-like structures appears at room temperature in the form of translational boundaries. Because of the random positioning of the initial nucleation of *Pbam* domains at high temperature, the inevitable outcome is the formation of translational boundaries. Based on this, we believe that the translational boundaries are important sources of the *Ima*2-like structures in PZO.

Having these results of heating and cooling, we would also like to discuss the possible impact of the model-predicted energy errors of certain phases on the finite-temperature simulations. As mentioned before, the model over stabilizes the $R3c$ phase by about 5.0 meV/f.u. (Table I), resulting in the model to incorrectly assign the ground state as the $R3c$ phase. Despite of this error, the global transitions from *Pbam*-AFE40, *Pnam*-AFE80 or *Ima*2-FiE to $R3c$ have never been observed. This may be due to the fact that the energy errors are so minor compared to the energy barriers between these phases. Another important reason is that the determinant for finite-temperature phase transitions is the free-energy, where the contribution not only involves internal energy but also underscores the crucial role of entropy. At higher temperatures, the role of entropy becomes even more significant. Our model can provide phonon density of states highly consistent with DFPT calculations (Fig. 6), indicating that the model can provide a quite good estimation of the lattice vibration entropy. By these considerations, we speculate that the over stabilization of the $R3c$ phase may lead to the overestimation of the temperature for the $R3c$ to *Pbam* transition (no experimental result from bulk samples available for comparison), and other than that the impact should be very limited.

B. Double *P-E* hysteresis loop

Finally, we utilize the model to investigate the electric field induce transitions at finite-temperature. We first point out that obtaining a typical double *P-E* hysteresis loop in PZO requires specific finite-temperature conditions. This is because the ferroelectric $R3c$ phase is dynamically stable [Fig. 6(c)] and possesses a large polarization at zero field [Fig. 7(c)], which contradicts the zero remnant polarization for a typical double hysteresis loop. The optimal temperature for the double *P-E* hysteresis loop should be slightly higher than the $R3c$ to *Pbam* transition temperature [approximately 420 K according to Fig. 7(c), although this value might be overestimated by the model]. At this temperature, the polar $R3c$ phase is destabilized under zero field but can be readily induced by the application of an electric field, and the nonpolar *Pbam*-AFE40 phase can be restored upon removing the electric field.

Figure 9 shows the simulation of double *P-E* hysteresis loop at 440 K. The electric field was applied along the pseudocubic [111] direction, following a triangle waveform as the shown in Fig. 9(c). The simulation provides a double *P-E* hysteresis loop nearly ideal for antiferroelectrics [Fig. 9(a)]. The maximum polarization $P_{max} = 0.514$ C/m² (at $E_{max} = 346$ kV/cm) is close to the experimental values, and the transition electric fields $E_{AFE-to-FE} \approx 200$ kV/cm and $E_{FE-to-AFE} \approx 70$ kV/cm are in the same order of magnitude with the experimental measurements on the PZO films [18,87,88]. Along with the double *P-E* hysteresis loop, the simulation also provides a sprout-shaped hysteresis loop for the strain, whose shape and the magnitude are also comparable with the experimental measurements on PZO-based materials [16,37].

In addition to successfully reproducing the polarization and electric-field induced strain properties, the model-based simulation also reveals the detailed atomic-scale processes of the PZO response to the electric fields. The changes of Pb displacements and the oxygen octahedra rotation are shown
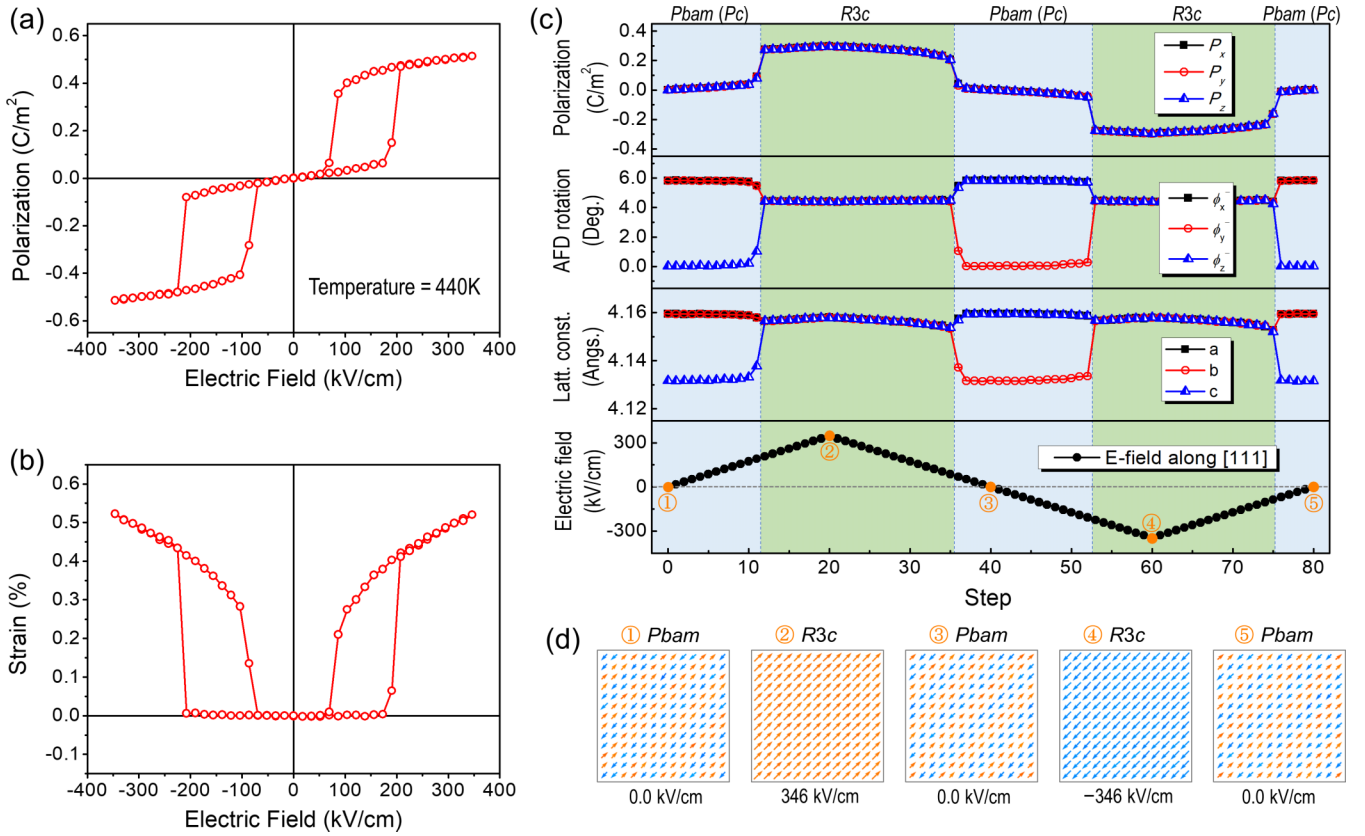
FIG. 9. Electric-field induced switching between AFE and FE phases. (a) Polarization hysteresis loop, and (b) strain hysteresis loop. The polarization was projected into the direction of the electric field, and the strain represents the normal strain component along the direction of the electric field. (c) Changes of polarization, oxygen octahedra antiphase rotations, lattice constants during the cycling of the electric field. (d) Local Pb displacement maps from the average structure at different stages of the application of electric field. The arrows represent local Pb displacements with respect to the average position of the 12 surrounding oxygen atoms, with colors indicating directions. The simulations were performed using a $12 \times 12 \times 12$ supercell at 440 K, and the electric field is applied along pseudocubic [111] direction.

in Figs. 9(c) and 9(d), from which the switching between *Pbam*-AFE40 ($a^-a^-c^0$, ↑↑↓↓) and *R*3*c* ($a^-a^-a^-$, ↑↑↑↑) during the cycling of electric field is quite clear. Given that numerous functionalities of PZO, such as dielectric energy storage, electromechanical actuation, electrocaloricity, thermal switching, etc., are all closely linked to electric-field induced AFE-FE transitions, the model also emerges as a potent tool to elucidate the atomistic mechanisms underlying these functionalities.

V. CONCLUSION

We have developed a deep-learning interatomic potential for the prototype antiferroelectric perovskite PZO, and demonstrated the capabilities of the model in simulating properties of relatively large systems at finite temperatures and finite electric fields. The successes of the model include: (1) describing a large number of phases, especially the recently discovered *Pnam*-AFE80 and *Ima*2-FiE, and accurately predicting structural and dynamical properties; (2) providing *Pbam* to cubic phase transition temperatures close to the experimental measurement ($T_C^{\text{model}} \approx 480$ K, $T_C^{\text{exp.}} \approx 505$ K); (3) producing double polarization hysteresis loop that closely resembles the experimental measurement. The primary weakness of the model is the underestimation of the energy of *R*3*c*

phase by about 5.0 meV/f.u. As a result, the temperature of the transition from *R*3*c* to *Pbam* is likely overestimated.

In this study, the key physical insight provided by the model concerns the formation of *Pbam* and *Ima*2 structures during cooling. Our atomistic simulation shows that at the temperature just below T_C, the *Pbam*-AFE40 exhibits a free-energy advantage over the other phases. For this reason, the *Pbam*-like structure appears first, and then frozen down to low temperatures, while the global transition from *Pbam*-AFE40 to *Ima*2-FiE is probably kinetically hindered. The *Ima*2 structure is more likely to appears locally in the form of translational boundaries. Due to the stochastic nature of the nucleation of *Pbam* domains just below T_C, the formation of translational boundaries at low temperatures is almost inevitable, making them an important source of *Ima*2 structures in PZO.

These results also demonstrate the effectiveness and power of the model-based large-scale atomistic simulations. Through these simulations, not only the macroscopic behaviors comparable to experiments can be reproduced, but also the microscale atomistic mechanisms can be accessed. We prospect that this model will serve as a valuable tool for studying a variety of intriguing phenomena in PZO, including translational boundaries, ferroelastic domain walls, and topological polar structures, as well as functional properties related

to energy storage, electric-field induced strain, electrocaloric effect, and thermal switching, etc.

APPENDIX: LATTICE PARAMETERS, ELASTIC AND PIEZOELECTRIC TENSORS OF DIFFERENT PHASES OF PZO

Tables II–IV provide comparisons of lattice parameters, elastic and piezoelectric tensors of various phases obtained from both first-principles and model-based calculations, respectively, serving as validations of the model. Since some of the data have not been previously reported, these tables may also serve as valuable references for future research.

TABLE II. Lattice parameters of different phases of PZO.

	Phase	DFT			Model			Error		
		a (Å)	b (Å)	c (Å)	a (Å)	b (Å)	c (Å)	a (%)	b (%)	c (%)
1	$Pm\bar{3}m$	4.1402	4.1402	4.1402	4.1401	4.1401	4.1401	−0.001	−0.001	−0.001
2	$P4mm$	4.1121	4.1121	4.2579	4.1102	4.1102	4.2630	−0.046	−0.046	0.121
3	$Amm2$	4.1129	5.8607	5.9957	4.1129	5.8624	5.9929	0.001	0.030	−0.046
4	$R3m$	5.8675	5.8675	7.2985	5.8665	5.8665	7.2998	−0.016	−0.016	0.018
5	$Pmma$-X	8.3166	4.1523	4.1548	8.3178	4.1534	4.1545	0.014	0.026	−0.007
6	$Cmcm$-AFE	5.8156	5.9437	8.3170	5.8153	5.9460	8.3162	−0.005	0.039	−0.010
7	$Cmmm$	8.3155	8.4144	4.0968	8.3140	8.4158	4.0955	−0.017	0.017	−0.031
8	$Pmma$-M	5.8641	4.0971	5.9770	5.8655	4.0967	5.9766	0.024	−0.011	−0.006
9	$P4/nmm$	5.8636	5.8636	4.1415	5.8652	5.8652	4.1408	0.026	0.026	−0.018
10	$I4/mmm$-AFE	5.8846	5.8846	8.3014	5.8844	5.8844	8.3016	−0.004	−0.004	0.002
11	$R\bar{3}m$	5.8652	5.8652	14.5461	5.8647	5.8647	14.5521	−0.009	−0.009	0.041
12	$P4/mbm$	5.7711	5.7711	4.1855	5.7709	5.7709	4.1851	−0.003	−0.003	−0.010
13	$I4/mcm$	5.7715	5.7715	8.3574	5.7691	5.7691	8.3616	−0.041	−0.041	0.050
14	$I4/mmm$-AFD	8.2663	8.2663	8.1813	8.2633	8.2633	8.1860	−0.037	−0.037	0.058
15	$Cmcm$-AFD	8.1592	8.2638	8.2636	8.1570	8.2636	8.2650	−0.027	−0.003	0.017
16	$Imma$	5.8233	8.1535	5.8685	5.8208	8.1514	5.8711	−0.044	−0.025	0.044
17	$Im\bar{3}$	8.2415	8.2415	8.2415	8.2416	8.2416	8.2416	0.002	0.002	0.002
18	$P4_2/nmc$	8.2091	8.2091	8.2784	8.2085	8.2085	8.2753	−0.007	−0.007	−0.038
19	$Pnma$	5.8261	8.2175	5.8076	5.8304	8.2105	5.8093	0.075	−0.085	0.030
20	$R\bar{3}c$	5.8403	5.8403	14.1540	5.8394	5.8394	14.1557	−0.015	−0.015	0.012
21	$P4bm$	5.7830	5.7830	4.2434	5.7837	5.7837	4.2416	0.011	0.011	−0.044
22	$I4cm$	5.7810	5.7810	8.4637	5.7818	5.7818	8.4608	0.015	0.015	−0.035
23	$R3$	11.7182	11.7182	7.2440	11.7173	11.7173	7.2352	−0.008	−0.008	−0.122
24	$R3c$	5.8412	5.8412	14.4261	5.8413	5.8413	14.4347	0.001	0.001	0.059
25	$Ima2$-FE	8.1766	5.8811	5.9050	8.1754	5.8810	5.9065	−0.014	0.000	0.027
26	$Pmna$	8.1279	5.8677	5.8903	8.1272	5.8651	5.8910	−0.009	−0.046	0.012
27	$Pbam$-II	11.7915	5.9623	4.1046	11.7941	5.9627	4.1030	0.022	0.008	−0.040
28	$Pbam$-AFE40	5.8742	11.7682	8.1723	5.8760	11.7663	8.1724	0.030	−0.016	0.002
29	$Pnam$-AFE80	5.8714	16.3651	11.7577	5.8732	16.3664	11.7556	0.032	0.008	−0.019
30	$Ima2$-FiE	8.1807	17.6294	5.8618	8.1789	17.6303	5.8640	−0.022	0.005	0.037

TABLE III. Elastic stiffness (unit: GPa) calculated by DFPT and the model for different phases of PZO.

	DFPT	Model
$Pm\bar{3}m$	$\begin{pmatrix} 325.6 & 91.5 & 91.5 & & & \\ 91.5 & 325.6 & 91.5 & & & \\ 91.5 & 91.5 & 325.6 & & & \\ & & & 64.8 & & \\ & & & & 64.8 & \\ & & & & & 64.8 \end{pmatrix}$	$\begin{pmatrix} 317.9 & 92.3 & 92.3 & & & \\ 92.3 & 317.9 & 92.3 & & & \\ 92.3 & 92.3 & 317.9 & & & \\ & & & 60.5 & & \\ & & & & 60.5 & \\ & & & & & 60.5 \end{pmatrix}$
$Imma$	$\begin{pmatrix} 281.5 & 129.0 & 112.2 & & & \\ 129.0 & 256.1 & 82.3 & & & \\ 112.2 & 82.3 & 285.3 & & & \\ & & & 66.0 & & \\ & & & & 66.5 & \\ & & & & & 67.4 \end{pmatrix}$	$\begin{pmatrix} 279.1 & 133.2 & 109.2 & & & \\ 133.2 & 257.4 & 79.1 & & & \\ 109.2 & 79.1 & 285.2 & & & \\ & & & 67.5 & & \\ & & & & 65.7 & \\ & & & & & 64.1 \end{pmatrix}$
$R3c$	$\begin{pmatrix} 217.5 & 100.7 & 56.5 & -11.0 & & \\ 100.7 & 217.5 & 56.5 & 11.0 & & \\ 56.5 & 56.5 & 145.3 & & & \\ -11.0 & 11.0 & & 46.0 & & \\ & & & & 46.0 & -11.0 \\ & & & & -11.0 & 58.4 \end{pmatrix}$	$\begin{pmatrix} 218.3 & 104.0 & 61.0 & -9.3 & & \\ 104.0 & 218.3 & 61.0 & 9.3 & & \\ 61.0 & 61.0 & 155.7 & & & \\ -9.3 & 9.3 & & 49.3 & & \\ & & & & 49.3 & -9.3 \\ & & & & -9.3 & 57.1 \end{pmatrix}$
$Pbam$-AFE40	$\begin{pmatrix} 260.6 & 86.9 & 96.9 & & & \\ 86.9 & 176.7 & 63.2 & & & \\ 96.9 & 63.2 & 231.3 & & & \\ & & & 58.3 & & \\ & & & & 66.8 & \\ & & & & & 73.0 \end{pmatrix}$	$\begin{pmatrix} 248.8 & 81.5 & 90.5 & & & \\ 81.5 & 174.7 & 58.4 & & & \\ 90.5 & 58.4 & 234.4 & & & \\ & & & 57.6 & & \\ & & & & 65.5 & \\ & & & & & 70.9 \end{pmatrix}$
$Pnam$-AFE80	$\begin{pmatrix} 247.3 & 79.7 & 105.4 & & & \\ 79.7 & 173.7 & 70.4 & & & \\ 105.4 & 70.4 & 220.7 & & & \\ & & & 59.9 & & \\ & & & & 66.7 & \\ & & & & & 74.1 \end{pmatrix}$	$\begin{pmatrix} 237.6 & 75.5 & 99.5 & & & \\ 75.5 & 170.8 & 64.4 & & & \\ 99.5 & 64.4 & 217.2 & & & \\ & & & 59.9 & & \\ & & & & 65.0 & \\ & & & & & 71.5 \end{pmatrix}$
$Ima2$-FiE	$\begin{pmatrix} 257.1 & 86.2 & 101.5 & & & \\ 86.2 & 183.6 & 72.4 & & & \\ 101.5 & 72.4 & 229.6 & & & \\ & & & 59.2 & & \\ & & & & 68.0 & \\ & & & & & 75.0 \end{pmatrix}$	$\begin{pmatrix} 247.1 & 79.6 & 96.2 & & & \\ 79.6 & 178.7 & 68.4 & & & \\ 96.2 & 68.4 & 231.7 & & & \\ & & & 60.2 & & \\ & & & & 65.3 & \\ & & & & & 71.6 \end{pmatrix}$

TABLE IV. Piezoelectric tensor (e-type, unit: C/m^2) calculated by DFPT and the model for the polar $R3c$ and $Ima2$-FiE phases of PZO.

	DFPT	Model
$R3c$	$\begin{pmatrix} & & & & 4.2 & 2.1 \\ 2.1 & -2.1 & & 4.2 & & \\ 3.0 & 3.0 & 3.7 & & & \end{pmatrix}$	$\begin{pmatrix} & & & & 4.1 & 2.0 \\ 2.0 & -2.0 & & 4.1 & & \\ 2.6 & 2.6 & 3.5 & & & \end{pmatrix}$
$Ima2$-FiE	$\begin{pmatrix} & & & & & 2.0 \\ 1.3 & 1.4 & -0.08 & & 0.0 & \\ & & & 0.65 & & \end{pmatrix}$	$\begin{pmatrix} & & & & & 1.6 \\ 1.2 & 1.6 & -0.15 & & 0.0 & \\ & & & 0.50 & & \end{pmatrix}$

[1] K. M. Rabe, Antiferroelectricity in oxides: A reexamination, in *Functional Metal Oxides*, edited by S. B. Ogale, T. V. Venkatesan, and M. G. Blamire (John Wiley & Sons, Hoboken, NJ, 2013), pp. 221–244.

[2] M. E. Lines and A. M. Glass, *Principles and Applications of Ferroelectrics and Related Materials* (Oxford University Press, New York, 1977).

[3] X. Tan, C. Ma, J. Frederick, S. Beckman, and K. G. Webber, The antiferroelectric ↔ ferroelectric phase transition in lead-containing and lead-free perovskite ceramics, J. Am. Ceram. Soc. **94**, 4091 (2011).

[4] L. Jin, F. Li, and S. Zhang, Decoding the fingerprint of ferroelectric loops: Comprehension of the material properties and structures, J. Am. Ceram. Soc. **97**, 1 (2014).

[5] X. Hao, J. Zhai, L. B. Kong, and Z. Xu, A comprehensive review on the progress of lead zirconate-based antiferroelectric materials, Prog. Mater. Sci. **63**, 1 (2014).

[6] Z. Liu, T. Lu, J. Ye, G. Wang, X. Dong, R. Withers, and Y. Liu, Antiferroelectrics for energy storage applications: A review, Adv. Mater. Technol. **3**, 1800111 (2018).

[7] Y. Si, T. Zhang, C. Liu, S. Das, B. Xu, R. G. Burkovsky, X.-K. Wei, and Z. Chen, Antiferroelectric oxide thin-films: Fundamentals, properties, and applications, Prog. Mater. Sci. **142**, 101231 (2024).

[8] C. Kittel, Theory of antiferroelectric crystals, Phys. Rev. **82**, 729 (1951).

[9] G. Shirane, E. Sawaguchi, and Y. Takagi, Dielectric properties of lead zirconate, Phys. Rev. **84**, 476 (1951).

[10] E. Sawaguchi, H. Maniwa, and S. Hoshino, Antiferroelectric structure of lead zirconate, Phys. Rev. **83**, 1078 (1951).

[11] C. A. Randall, Z. Fan, I. Reaney, L.-Q. Chen, and S. Trolier-McKinstry, Antiferroelectrics: History, fundamentals, crystal chemistry, crystal structures, size effects, and applications, J. Am. Ceram. Soc. **104**, 3775 (2021).

[12] G. Wang, Z. Lu, Y. Li, L. Li, H. Ji, A. Feteira, D. Zhou, D. Wang, S. Zhang, and I. M. Reaney, Electroceramics for high-energy density capacitors: Current status and future perspectives, Chem. Rev. **121**, 6124 (2021).

[13] D. Li, X. Meng, E. Zhou, X. Chen, Z. Shen, Q. Guo, Z. Yao, M. Cao, J. Wu, S. Zhang, H. Liu, and H. Hao, Ultrahigh energy density of antiferroelectric $PbZrO_3$-based films at low electric field, Adv. Funct. Mater. **33**, 2302995 (2023).

[14] K. Uchino, Antiferroelectric shape memory ceramics, Actuators **5**, 11 (2016).

[15] H. Pan, M. Zhu, E. Banyas, L. Alaerts, M. Acharya, H. Zhang, J. Kim, X. Chen, X. Huang, M. Xu *et al.*, Clamping enables enhanced electromechanical responses in antiferroelectric thin films, Nat. Mater. **23**, 944 (2024).

[16] J. Frederick, X. Tan, and W. Jo, Strains and polarization during antiferroelectric–ferroelectric phase switching in $Pb_{0.99}Nb_{0.02}[(Zr_{0.57}Sn_{0.43})_{1-y}Ti_y]_{0.98}O_3$ ceramics, J. Am. Ceram. Soc. **94**, 1149 (2011).

[17] A. S. Mischenko, Q. Zhang, J. F. Scott, R. W. Whatmore, and N. D. Mathur, Giant electrocaloric effect in thin-film $PbZr_{0.95}Ti_{0.05}O_3$, Science **311**, 1270 (2006).

[18] C. Liu, Y. Si, H. Zhang, C. Wu, S. Deng, Y. Dong, Y. Li, M. Zhuo, N. Fan, B. Xu, P. Lu, L. Zhang *et al.*, Low voltage driven high-performance thermal switching in antiferroelectric $PbZrO_3$ thin films, Science **382**, 1265 (2023).

[19] A. M. Glazer, K. Roleder, and J. Dec, Structure and disorder in single-crystal lead zirconate, $PbZrO_3$, Acta Cryst. B **49**, 846 (1993).

[20] E. Sawaguchi, G. Shirane, and Y. Takagi, Phase transition in lead zirconate, J. Phys. Soc. Jpn. **6**, 333 (1951).

[21] H. Fujishita and S. Hoshino, A study of structural phase transitions in antiferroelectric $PbZrO_3$ by neutron diffraction, J. Phys. Soc. Jpn. **53**, 226 (1984).

[22] Z. Xu, X. Dai, D. Viehland, D. A. Payne, Z. Li, and Y. Jiang, Ferroelectric domains and incommensuration in the intermediate phase region of lead zirconate, J. Am. Ceram. Soc. **78**, 2220 (1995).

[23] H. Liu, Origin of the intermediate phase in lead zirconate, $PbZrO_3$, J. Am. Ceram. Soc. **101**, 5281 (2018).

[24] B. Xu, O. Hellman, and L. Bellaiche, Order-disorder transition in the prototypical antiferroelectric $PbZrO_3$, Phys. Rev. B **100**, 020102(R) (2019).

[25] Z. An, H. Yokota, N. Zhang, M. Paściak, J. Fábry, M. Kopecký, J. Kub, G. Zhang, A. M. Glazer, T. R. Welberry, W. Ren, and Z.-G. Ye, Multiple structural components and their competition in the intermediate state of antiferroelectric $Pb(Zr, Ti)O_3$, Phys. Rev. B **103**, 054113 (2021).

[26] H. Aramberri, C. Cazorla, M. Stengel, and J. Íñiguez, On the possibility that $PbZrO_3$ not be antiferroelectric, npj Comput. Mater. **7**, 196 (2021).

[27] J. S. Baker, M. Paściak, J. K. Shenton, P. Vales-Castro, B. Xu, J. Hlinka, P. Márton, R. G. Burkovsky, G. Catalan, and A. M. Glazer, A re-examination of antiferroelectric $PbZrO_3$ and $PbHfO_3$: An 80-atom *Pnam* structure, arXiv:2102.08856.

[28] Y. Liu, R. Niu, A. Majchrowski, K. Roleder, K. Cordero-Edwards, J. M. Cairney, J. Arbiol, and G. Catalan, Translational boundaries as incipient ferrielectric domains in antiferroelectric $PbZrO_3$, Phys. Rev. Lett. **130**, 216801 (2023).

[29] R.-J. Jiang, Y. Cao, W.-R. Geng, M.-X. Zhu, Y.-L. Tang, Y.-L. Zhu, Y. Wang, F. Gong, S.-Z. Liu, Y.-T. Chen, J. Liu, N. Liu, J.-H. Wang, X.-D. Lv, S.-J. Chen, and X.-L. Ma, Atomic insight into the successive antiferroelectric-ferroelectric phase transition in antiferroelectric oxides, Nano Lett. **23**, 1522 (2023).

[30] Z. Yu, N. Fan, Z. Fu, B. He, S. Yan, H. Cai, X. Chen, L. Zhang, Y. Zhang, B. Xu, G. Wang, and F. Xu, Room-temperature stabilizing strongly competing ferrielectric and antiferroelectric phases in $PbZrO_3$ by strain-mediated phase separation, Nat. Commun. **15**, 3438 (2024).

[31] S. E. Reyes-Lillo and K. M. Rabe, Antiferroelectricity and ferroelectricity in epitaxially strained $PbZrO_3$ from first principles, Phys. Rev. B **88**, 180102(R) (2013).

[32] S. Amisi, Ab initio investigation in $PbZrO_3$ antiferroelectric: Structural and vibrational properties, Eur. Phys. J. Plus **136**, 653 (2021).

[33] O. E. Fesenko, R. V. Kolesova, and Y. G. Sindeyev, The structural phase transitions in lead zirconate in super-high electric fields, Ferroelectrics **20**, 177 (1978).

[34] R. G. Burkovsky, G. A. Lityagin, A. E. Ganzha, A. F. Vakulenko, R. Gao, A. Dasgupta, B. Xu, A. V. Filimonov, and L. W. Martin, Field-induced heterophase state in $PbZrO_3$ thin films, Phys. Rev. B **105**, 125409 (2022).

[35] C. Liu, Y. Si, M. Hao, Y. Tao, S. Deng, P. Lu, C. Zhao, Z. Chen, G. Zhang, and Y. Chen, Phonon entropy engineering for caloric cooling, Appl. Phys. Rev. **10**, 031411 (2023).

[36] P. Dufour, T. Maroutian, M. Vallet, K. Patel, A. Chanthbouala, C. Jacquemont, L. Yedra, V. Humbert, F. Godel, B. Xu, S. Prosandeev *et al.*, Ferroelectric phase transitions in epitaxial antiferroelectric $PbZrO_3$ thin films, Appl. Phys. Rev. **10**, 021405 (2023).

[37] S.-E. Park, M.-J. Pan, K. Markowski, S. Yoshikawa, and L. E. Cross, Electric field induced phase transition of antiferroelectric lead lanthanum zirconate titanate stannate ceramics, J. Appl. Phys. **82**, 1798 (1997).

[38] H. He and X. Tan, Electric-field-induced transformation of incommensurate modulations in antiferroelectric $Pb_{0.99}Nb_{0.02}[(Zr_{1-x}Sn_x)_{1-y}Ti_y]O_3$, Phys. Rev. B **72**, 024102 (2005).

[39] Z. Li, Z. Fu, H. Cai, T. Hu, Z. Yu, Y. Luo, L. Zhang, H. Yao, X. Chen, S. Zhang, G. Wang, X. Dong, and F. Xu, Discovery

of electric devil's staircase in perovskite antiferroelectric, Sci. Adv. **8**, eabl9088 (2022).

[40] X. Tan, J. Frederick, C. Ma, W. Jo, and J. Rödel, Can an electric field induce an antiferroelectric phase out of a ferroelectric phase? Phys. Rev. Lett. **105**, 255702 (2010).

[41] H. Guo and X. Tan, Direct observation of the recovery of an antiferroelectric phase during polarization reversal of an induced ferroelectric phase, Phys. Rev. B **91**, 144104 (2015).

[42] H. Liu, L. Fan, S. Sun, K. Lin, Y. Ren, X. Tan, X. Xing, and J. Chen, Electric-field-induced structure and domain texture evolution in PbZrO$_3$-based antiferroelectric by *in-situ* high-energy synchrotron X-ray diffraction, Acta Mater. **184**, 41 (2020).

[43] Z. An, H. Yokota, K. Kurihara, N. Hasegawa, P. Marton, A. M. Glazer, Y. Uesu, W. Ren, Z.-G. Ye, M. Paściak, and N. Zhang, Tuning of polar domain boundaries in nonpolar perovskite, Adv. Mater. **35**, 2207665 (2023).

[44] P. Ghosez and J. Junquera, Modeling of ferroelectric oxide perovskites: From first to second principles, Annu. Rev. Condens. Matter Phys. **13**, 325 (2022).

[45] B. K. Mani, S. Lisenkov, and I. Ponomareva, Finite-temperature properties of antiferroelectric PbZrO$_3$ from atomistic simulations, Phys. Rev. B **91**, 134112 (2015).

[46] K. Patel, B. Xu, S. Prosandeev, R. Faye, B. Dkhil, P.-E. Janolin, and L. Bellaiche, Temperature-dependent properties of the antiferroelectric model PbZrO$_3$: An effective Hamiltonian study, Phys. Rev. B **106**, 214108 (2022).

[47] O. Gindele, A. Kimmel, M. G. Cain, and D. Duffy, Shell model force field for lead zirconate titanate Pb(Zr$_{1-x}$Ti$_x$)O$_3$, J. Phys. Chem. C **119**, 17784 (2015).

[48] M. Paściak, T. R. Welberry, A. P. Heerdegen, V. Laguta, T. Ostapchuk, S. Leoni, and A. J. Hlinka, Atomistic modeling of diffuse scattering in cubic PbZrO$_3$, Phase Trans. **88**, 273 (2015).

[49] O. T. Unke, S. Chmiela, H. E. Sauceda, M. Gastegger, I. Poltavsky, K. T. Schütt, A. Tkatchenko, and K.-R. Müller, Machine learning force fields, Chem. Rev. **121**, 10142 (2021).

[50] T. Wen, L. Zhang, H. Wang, W. E, and D. J. Srolovitz, Deep potentials for materials science, Mater. Futures **1**, 022601 (2022).

[51] L. Zhang, J. Han, H. Wang, R. Car, and W. E, Deep potential molecular dynamics: A scalable model with the accuracy of quantum mechanics, Phys. Rev. Lett. **120**, 143001 (2018).

[52] L. Zhang, H. Wang, R. Car, and W. E, Phase diagram of a deep potential water model, Phys. Rev. Lett. **126**, 236001 (2021).

[53] L. Zhang, D.-Y. Lin, H. Wang, R. Car, and W. E, Active learning of uniformly accurate interatomic potentials for materials simulation, Phys. Rev. Mater. **3**, 023804 (2019).

[54] R. Li, Z. Liu, A. Rohskopf, K. Gordiz, A. Henry, E. Lee, and T. Luo, A deep neural network interatomic potential for studying thermal conductivity of β-Ga$_2$O$_3$, Appl. Phys. Lett. **117**, 152102 (2020).

[55] J. Zeng, L. Cao, M. Xu, T. Zhu, and J. Z. H. Zhang, Complex reaction processes in combustion unraveled by neural network-based molecular dynamics simulation, Nat. Commun. **11**, 5713 (2020).

[56] R. He, H. Wu, L. Zhang, X. Wang, F. Fu, S. Liu, and Z. Zhong, Structural phase transitions in SrTiO$_3$ from deep potential molecular dynamics, Phys. Rev. B **105**, 064104 (2022).

[57] H.-C. Thong, XiaoYang Wang, J. Han, L. Zhang, B. Li, K. Wang, and B. Xu, Machine learning interatomic potential for molecular dynamics simulation of the ferroelectric KNbO$_3$ perovskite, Phys. Rev. B **107**, 014101 (2023).

[58] P. Xie, Y. Chen, and R. Car, Ab initio multi-scale modeling of ferroelectrics: The case of PbTiO$_3$, arXiv:2205.11839.

[59] Y. Shi, R. He, B. Zhang, and Z. Zhong, Revisiting the phase diagram and piezoelectricity of lead zirconate titanate from first principles, Phys. Rev. B **109**, 174104 (2024).

[60] J. Wu, Y. Zhang, L. Zhang, and S. Liu, Deep learning of accurate force field of ferroelectric HfO$_2$, Phys. Rev. B **103**, 024108 (2021).

[61] Z. Gong, J. Z. Liu, X. Ding, J. Sun, and J. Deng, Strain-aided room-temperature second-order ferroelectric phase transition in monolayer PbTe: Deep potential molecular dynamics simulations, Phys. Rev. B **108**, 134112 (2023).

[62] J. Wu, L. Bai, J. Huang, L. Ma, J. Liu, and S. Liu, Accurate force field of two-dimensional ferroelectrics from deep learning, Phys. Rev. B **104**, 174107 (2021).

[63] R. He, B. Zhang, H. Wang, L. Li, P. Tang, G. Bauer, and Z. Zhong, Ultrafast switching dynamics of the ferroelectric order in stacking-engineered ferroelectrics, Acta Mater. **262**, 119416 (2024).

[64] J. Wu, J. Yang, L. Ma, L. Zhang, and S. Liu, Modular development of deep potential for complex solid solutions, Phys. Rev. B **107**, 144102 (2023).

[65] J. Wu, J. Yang, Y.-J. Liu, D. Zhang, Y. Yang, Y. Zhang, L. Zhang, and S. Liu, Universal interatomic potential for perovskite oxides, Phys. Rev. B **108**, L180104 (2023).

[66] X. Gonze, B. Amadon, G. Antonius, F. Arnardi, L. Baguet, J.-M. Beuken, J. Bieder, F. Bottin, J. Bouchet, E. Bousquet, N. Brouwer, F. Bruneval, G. Brunin, T. Cavignac, J.-B. Charraud, W. Chen *et al.*, The ABINIT project: Impact, environment and recent developments, Comput. Phys. Commun. **248**, 107042 (2020).

[67] X. Gonze, F. Jollet, F. A. Araujo, D. Adams, B. Amadon, T. Applencourt, C. Audouze, J.-M. Beuken, J. Bieder, A. Bokhanchuk, E. Bousquet, F. Bruneval, and D. Caliste, Recent developments in the ABINIT software package, Comput. Phys. Commun. **205**, 106 (2016).

[68] X. Gonze, B. Amadon, P.-M. Anglade, J.-M. Beuken, F. Bottin, P. Boulanger, F. Bruneval, D. Caliste, R. Caracas, M. Côté *et al.*, ABINIT: First-principles approach to material and nanosystem properties, Comput. Phys. Commun. **180**, 2582 (2009).

[69] X. Gonze, J.-M. Beuken, R. Caracas, F. Detraux, M. Fuchs, G.-M. Rignanese, L. Sindic, M. Verstraete, G. Zerah, F. Jollet *et al.*, First-principles computation of material properties: The ABINIT software project, Comput. Mater. Sci. **25**, 478 (2002).

[70] J. P. Perdew, A. Ruzsinszky, G. I. Csonka, O. A. Vydrov, G. E. Scuseria, L. A. Constantin, X. Zhou, and K. Burke, Restoring the density-gradient expansion for exchange in solids and surfaces, Phys. Rev. Lett. **100**, 136406 (2008).

[71] M. J. van Setten, M. Giantomassi, E. Bousquet, M. J. Verstraete, D. R. Hamann, X. Gonze, and G.-M. Rignanese, The PSEUDODOJO: Training and grading a 85 element optimized norm-conserving pseudopotential table, Comput. Phys. Commun. **226**, 39 (2018).

[72] D. R. Hamann, Optimized norm-conserving Vanderbilt pseudopotentials, Phys. Rev. B **88**, 085117 (2013).

[73] X. Gonze and C. Lee, Dynamical matrices, Born effective charges, dielectric permittivity tensors, and interatomic force constants from density-functional perturbation theory, Phys. Rev. B **55**, 10355 (1997).

[74] https://github.com/mailhexu/dpdata_abinit.

[75] H. Wang, L. Zhang, J. Han, and W. E, DeePMD-kit: A deep learning package for many-body potential energy representation and molecular dynamics, Comput. Phys. Commun. **228**, 178 (2018).

[76] J. Zeng, D. Zhang, D. Lu, P. Mo, Z. Li, Y. Chen, M. Rynik, L. Huang, Z. Li, S. Shi, Y. Wang, H. Ye *et al.*, DeePMD-kit v2: A software package for deep potential models, J. Chem. Phys. **159**, 054801 (2023).

[77] S. Plimpton, Fast parallel algorithms for short-range molecular dynamics, J. Comput. Phys. **117**, 1 (1995).

[78] A. P. Thompson, H. M. Aktulga, R. Berger, D. S. Bolintineanu, W. M. Brown, P. S. Crozier, P. J. in 't Veld, A. Kohlmeyer, S. G. Moore, T. D. Nguyen *et al.*, LAMMPS—A flexible simulation tool for particle-based materials modeling at the atomic, meso, and continuum scales, Comput. Phys. Commun. **271**, 108171 (2022).

[79] A. Togo and I. Tanaka, First principles phonon calculations in materials science, Scr. Mater. **108**, 1 (2015).

[80] https://github.com/piti-diablotin/agate.

[81] Y. Zhang, H. Wang, W. Chen, J. Zeng, L. Zhang, H. Wang, and Weinan E, DP-GEN: A concurrent learning platform for the generation of reliable deep learning based potential energy models, Comput. Phys. Commun. **253**, 107206 (2020).

[82] L. Bastogne, J. Bieder, A. Martin, M. Schmitt, A. Sasani, H. Zhang, X. He, and P. Ghosez, MULTIBINIT-LATTICE: Toward automatized second-principles interatomic potentials (unpublished).

[83] R. E. Cohen, Origin of ferroelectricity in perovskite oxides, Nature (London) **358**, 136 (1992).

[84] L. Zhang, H. Wang, M. C. Muniz, A. Z. Panagiotopoulos, R. Car, and Weinan E, A deep potential model with long-range electrostatic interactions, J. Chem. Phys. **156**, 124107 (2022).

[85] Due to the tiny model underestimation of the internal energy of the $R3c$ phase, the transition temperature from $R3c$ to $Pbam$ might be slightly overestimated in our simulations.

[86] X.-K. Wei, A. K. Tagantsev, A. Kvasov, K. Roleder, C.-L. Jia, and N. Setter, Ferroelectric translational antiphase boundaries in nonpolar materials, Nat. Commun. **5**, 3031 (2014).

[87] J. Ge, D. Remiens, X. Dong, Y. Chen, J. Costecalde, F. Gao, F. Cao, and G. Wang, Enhancement of energy storage in epitaxial $PbZrO_3$ antiferroelectric films using strain engineering, Appl. Phys. Lett. **105**, 112908 (2014).

[88] J. Zhai and H. Chen, Direct current field and temperature dependent behaviors of antiferroelectric to ferroelectric switching in highly (100)-oriented $PbZrO_3$ thin films, Appl. Phys. Lett. **82**, 2673 (2003).